

Looking at the Sensitization of 11–12% Chromium EN 1.4003 Stainless Steels during Welding

Using a range of heat inputs and welding speeds, two steel grades with different austenite potentials were welded, and they were found to be sensitized when lower heat inputs and faster cooling rates suppressed austenite nucleation during cooling

BY M. L. GREEFF AND M. du TOIT

ABSTRACT. The susceptibility of 11–12% chromium type EN 1.4003 ferritic stainless steels to sensitization during continuous cooling after welding at low heat input levels was investigated. These steels transform partially to austenite in the high-temperature heat-affected zone (HTHAZ) during cooling, with the austenite transforming to martensite at lower temperatures. Two steel grades with different austenite potentials were welded using a range of heat inputs (30 to 450 J/mm) and welding speeds (2.36 to 33.3 mm/s). The steels were found to be sensitized when lower heat inputs and faster cooling rates suppressed austenite nucleation during cooling, resulting in almost fully ferritic heat-affected zones and continuous networks of ferrite-ferrite grain boundaries in the HTHAZ. With an increase in heat input, the cooling rate was reduced, and more martensite formed in the HTHAZ. The ferrite-martensite boundaries were generally observed to be unsensitized. The results suggest that if enough austenite forms in the HTHAZ during cooling, it acts as a carbon sink to dissolve excess carbon. This prevents supersaturation of the ferrite phase and subsequent carbide precipitation that could lead to sensitization of the ferrite grain boundaries. Excessive welding speeds appear to promote sensitization during low heat input welding.

Introduction

Low-carbon, 11 to 12% chromium fer-

M. L. GREEFF is a graduate student and M. du TOIT (mtoit@postino.up.ac.za) is an associate professor with the Department of Materials Science and Metallurgical Engineering, University of Pretoria, Pretoria, South Africa.

ritic stainless steels are used extensively in South Africa as low cost, utility stainless steels. These steels conform in composition to grades S41003 (ASTM A240) and 1.4003 (EN 10088-2 and EN 10028-7), with the specified chemical composition limits for these grades shown in Table 1. The EN 1.4003-type alloys perform well in many wet sliding abrasion applications and in aqueous environments, often replacing mild and galvanized steel in mildly corrosive surroundings (Refs. 1–3), and are widely used in the petrochemical, metallurgical, pulp, paper, coal, and sugar industries in materials handling and structural applications. The past few years have also seen a marked increase in the use of these steels in the transport, mining, and agricultural sectors, with successful application in passenger vehicles, coaches, buses, trucks, freight and passenger wagons, and rail infrastructure (Refs. 2, 3).

The EN 1.4003 ferritic stainless steels are designed to transform partially to austenite on cooling, passing through the dual-phase (austenite + ferrite) phase field on the Fe-Cr equilibrium phase diagram (shown in Fig. 1 for carbon contents below 0.01%). This partial solid-state phase transformation of ferrite to austenite during cooling improves the weldabil-

ity and as-welded toughness of these steels by restricting heat-affected zone grain growth (Refs. 4, 5). The alloys are usually supplied in the fully annealed and desensitized condition. During annealing (normally at temperatures between 700° and 750°C (Refs. 1, 2)), any austenite formed on cooling through the dual-phase region transforms completely to ferrite. Due to its low solubility in ferrite, the majority of the carbon precipitates as chromium-rich carbides or carbonitrides during annealing, but any chromium-depleted zones formed in the ferrite are healed through rapid chromium back-diffusion from the grain interiors.

The rapid cooling rates associated with welding, however, prevent the transformation of austenite to ferrite at lower temperatures, and any austenite formed on cooling through the dual-phase ($\delta + \gamma$) region transforms to low-carbon martensite below the M_s temperature (Ref. 4). The microstructure of the high-temperature heat-affected zone (HTHAZ) adjacent to the weld interface after cooling therefore usually consists of ferrite grains surrounded by grain boundary martensite. Despite the partial solid-state phase transformation from ferrite to austenite on cooling, the HTHAZ is normally characterized by grain growth. This is in contrast to the much finer grain size of the low-temperature heat-affected zone (LTHAZ) further removed from the weld interface.

Austenitic consumables are generally preferred for welding the EN 1.4003 alloys. Although this leads to a property mismatch between the weld and the surrounding base metal, the tough austenitic weld metal improves the overall toughness of the weld by absorbing some of the impact that the joint may be exposed to during service. A matching welding electrode is commercially available (classified as

KEYWORDS

EN 1.4003
High-Temperature Heat-Affected Zone (HTHAZ)
Ferrite-Ferrite Grain Boundaries
Stress Corrosion Cracking
Austenite

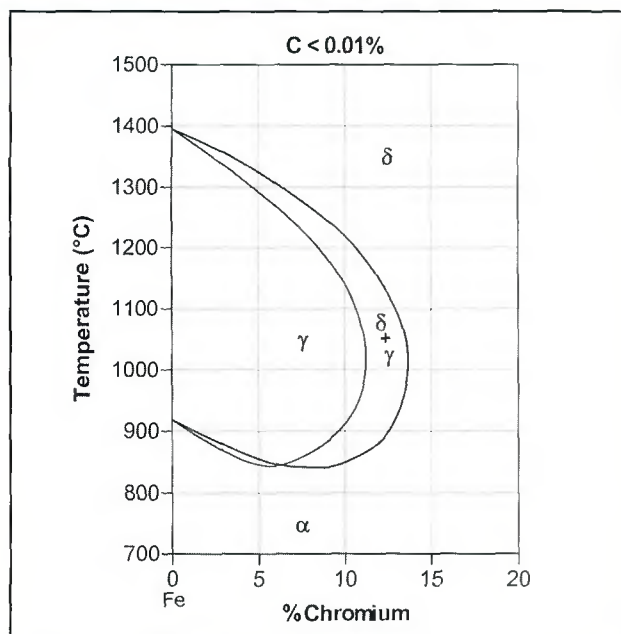


Fig. 1 — Vertical section of the ternary Fe-Cr-C system at carbon contents below 0.01%. Although the steels in this investigation contain more than 0.01% carbon, this phase diagram illustrates the general shape of the austenite and (austenite + ferrite) phase fields. An increase in carbon content is expected to enlarge these phase fields at the expense of ferrite (Ref. 6).

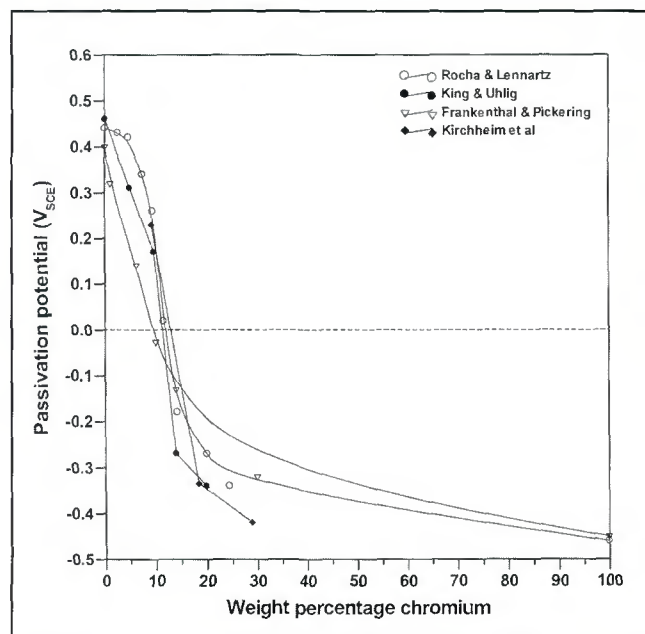


Fig. 2 — Passivation potential of binary iron-chromium alloys in 0.5 M H₂SO₄ at room temperature (Ref. 18), with data from Rocha and Lennartz (Ref. 19), King and Uhlig (Ref. 20), Frankenthal and Pickering (Ref. 21), and Kirchheim et al. (Ref. 22).

Table 1 — Specified Chemical Composition Limits for Grades S41003 (ASTM A240) and 1.4003 (EN 10088-2 and EN 10028-7) (% by mass, balance Fe)

Grade	C	Cr	Mn	Si	Ni	P	S	N
S41003	0.030 max.	10.5–12.5	1.50 max.	1.00 max.	1.50 max.	0.040 max.	0.030 max.	0.030 max.
1.4003	0.030 max.	10.5–12.5	1.50 max.	1.00 max.	0.30–1.00	0.040 max.	0.015 max.	0.030 max.

E410NiMo, with modified chromium content), but it is not recommended in applications where impact, shock, fatigue, or any other form of nonstatic loading is anticipated. This electrode is only specified in applications where matching corrosion resistance is essential.

A number of in-service failures of EN 1.4003 welds due to stress corrosion cracking in the high-temperature heat-affected zone adjacent to the weld interface have been reported in recent years (Ref. 7). Although it is frequently claimed that nickel-free stainless steels are immune to stress corrosion cracking, such failures have been reported in both nickel-free ferritic and martensitic stainless steels with corrosion potentials within the passive range (Refs. 8–10). The stress corrosion cracking of these stainless steels is generally believed to be associated with some degree of sensitization. Even though various sensitization models have been proposed for stainless steels, chromium depletion is the

most widely accepted mechanism (Ref. 11). This theory states that sensitization is caused by intergranular precipitation of chromium-rich M₂₃C₆-type carbides, resulting in chromium depletion of the matrix surrounding the precipitated particles. If chromium depletion reduces the chromium level in the affected areas to below the concentration required to maintain passivation, the steel becomes sensitized to intergranular corrosion.

It was originally believed that the typical dual-phase heat-affected zone microstructure that develops during welding renders the EN 1.4003-type steels largely immune to sensitization. The cooling rates during welding are generally considered to be too fast to cause sensitization of the austenite phase, whereas the ferrite phase is rapidly desensitized by chromium back-diffusion into depleted regions during cooling. This mechanism is similar to that proposed for the enhanced sensitization resistance observed in duplex austenitic-

ferritic stainless steels (Ref. 12). It has, however, since been confirmed that the EN 1.4003 steels are susceptible to sensitization under very specific conditions. The majority of the failures associated with stress corrosion cracking and sensitization in these steels were caused by a two-step thermal cycle. The first step involves heating the steel to a temperature within the (γ + δ) phase field above the carbide dissolution temperature (approximately 950°C). During this heating cycle, carbon liberated through the dissolution of the carbide precipitates is absorbed by the austenite phase. On cooling after welding, the austenite transforms to unsensitized martensite. If this martensite is subsequently heated to a temperature within the carbide precipitation range of approximately 550° to 850°C (the second step in the thermal cycle), sensitization of the martensite phase may occur. In the heat-affected zone, these conditions may be satisfied by an isothermal heat treatment above 950°C (step 1), followed by rapid cooling and welding (step 2), or by overlapping heat-affected zones in the case of multipass or closely spaced welds (Ref. 7).

The chromium depletion mechanism for sensitization in the EN 1.4003 steels has been confirmed using transmission electron microscopy with electron energy loss (EELS) image filtering. Sensitized material displays chromium enrichment along the grain boundaries, as well as distinctive chromium-depleted zones adjacent to the boundaries (Ref. 13). The in-

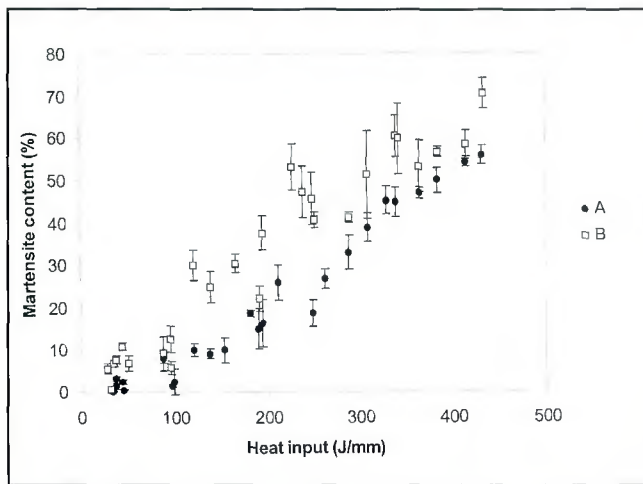


Fig. 3 — Measured HTHAZ martensite content of steels A and B as a function of heat input during welding.

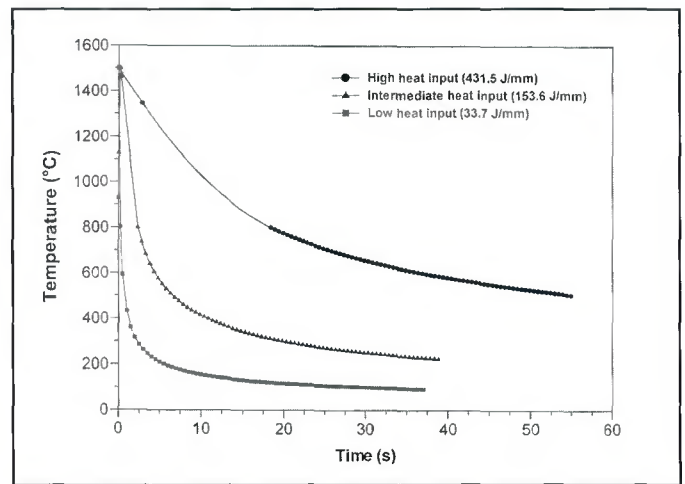


Fig. 4 — Calculated temperature-time profiles experienced by a point located on the weld interface for a “low” heat input weld (33.7 J/mm or 856 J/in., with a cooling time from 1500° to 800°C, Δt_{15-8} of 0.22 s), an “intermediate” heat input weld (153.6 J/mm or 3901 J/in., with a Δt_{15-8} of 2.08 s), and a “high” heat input weld (431.5 J/mm or 10960 J/in., with a Δt_{15-8} of 18.40 s).

Table 2 — The Chemical Compositions of the Two Type EN 1.4003 Alloys Examined during the Course of This Investigation (% by mass, balance Fe)

Steel	C	Cr	Mn	Si	Ni	Ti	N	KFF
A	0.018	11.61	0.56	0.70	0.33	0.032	0.0213	12.05
B	0.012	11.57	0.49	0.38	0.55	0.014	0.0177	9.59

Table 3 — Material Constants Supplied by Columbus Stainless for the EN 1.4003 Steels

Thermal diffusivity, a	$1.10819 \cdot 10^{-5} \text{ m}^2 \text{ s}^{-1}$
Thermal conductivity, λ	$41.0 \text{ Jm}^{-1} \text{ s}^{-1} \text{ K}^{-1}$

tergranular precipitation of chromium-rich carbides with associated grain boundary chromium depletion in dual-phase ferritic-martensitic 12 and 13% chromium steels has also been reported by Tomari et al. (Ref. 14) and Frangini et al. (Ref. 15).

A number of recent fillet weld failures attributed to stress corrosion cracking and sensitization suggested, however, that sensitization can also occur during continuous cooling after welding, without recourse to the two-step thermal cycle described above. These failures were associated with fast welding speeds and excessive fillet weld overlap, implying that low heat inputs play a role in promoting sensitization under these conditions. This investigation aimed to show that it is possible for the EN 1.4003-type steels to sensitize during continuous cooling after welding. The project also attempted to identify the mechanism of sensitization during low heat input welding, and to relate this phenomenon to the cooling rate and the heat-affected zone microstructure that develops during the weld thermal cycle.

Experimental Procedure

The chemical compositions of the EN 1.4003-type steels examined during the course of this investigation, designated steels A and B, are shown in Table 2. Both

steels conform in chemical composition to the specifications shown in Table 1 for grades S41003 and 1.4003. The Kaltenhauser ferrite factor (KFF), calculated from Equation 1 (Ref. 16), is included in Table 2 for both alloys. This factor quantifies the ratio of ferrite- to austenite-forming elements in the steel. As shown in Table 2, steel B has a lower ferrite factor, and consequently a higher austenite potential, than steel A. More austenite is therefore expected to form in the high-temperature heat-affected zone of steel B during cooling. The steels were supplied in the form of fully annealed and homogenized plate with a thickness of 3 mm.

$$\text{KFF} = \text{Cr} + 6\text{Si} + 8\text{Ti} + 4\text{Mo} + 2\text{Al} - 40(\text{C} + \text{N}) - 2\text{Mn} - 4\text{Ni} \quad (1)$$

In order to examine the influence of the welding parameters, and in particular the heat input and the welding speed on the microstructure and sensitization resistance of the high-temperature heat-affected zone adjacent to the weld interface, the alloys shown in Table 2 were welded autogenously using heat inputs ranging from about 30 to 450 J/mm (762 to 11430 J/in.) and welding speeds from 2.36 to 33.3 mm/s (5.6 to 78.7 in./min). Direct

current gas tungsten arc welding (GTAW) was used with argon shielding gas and electrode negative polarity. The welding parameters selected to produce the experimental welds are given in Tables 1 and II in the Appendix for alloys A and B, respectively. All the experimental welds were pickled and passivated using commercially available solutions.

Sensitization was evaluated using the 10% oxalic acid electrolytic etch described in Practice W of ASTM 763-93 (Ref. 17). In order to classify the resulting microstructures as ditched (possibly sensitized), dual (unsensitized), or step (unsensitized), the etched samples were examined using an optical microscope. The oxalic acid etch reveals the presence of any chromium-rich carbides in the microstructure, but only serves as a screening test for sensitization. In order to confirm that a sample with ditched grain boundaries after oxalic acid etching is in the sensitized condition, additional tests are required. The boiling acid tests described in ASTM 763-93 were found to be too aggressive for the 12% chromium EN 1.4003 steels, and confirmation of whether the heat-affected zones were in the sensitized condition was therefore obtained using a potentiostatic chromium depletion test performed in 0.5 M H_2SO_4 at 0 V_{SCE} (relative to a saturated calomel electrode)

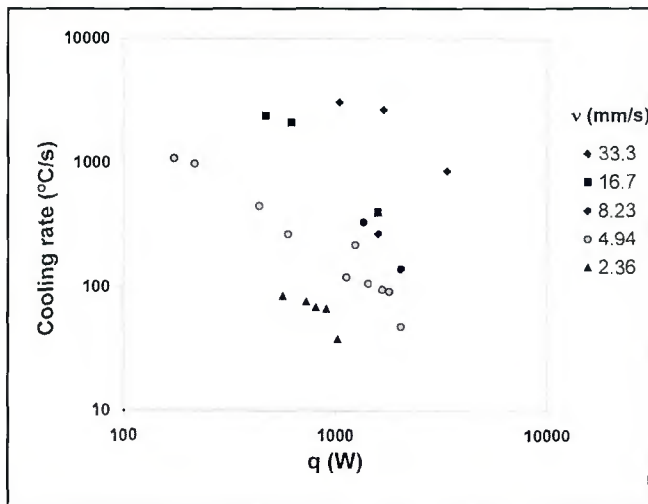


Fig. 5 — The influence of welding parameters on the cooling rate from 1500° to 800°C.

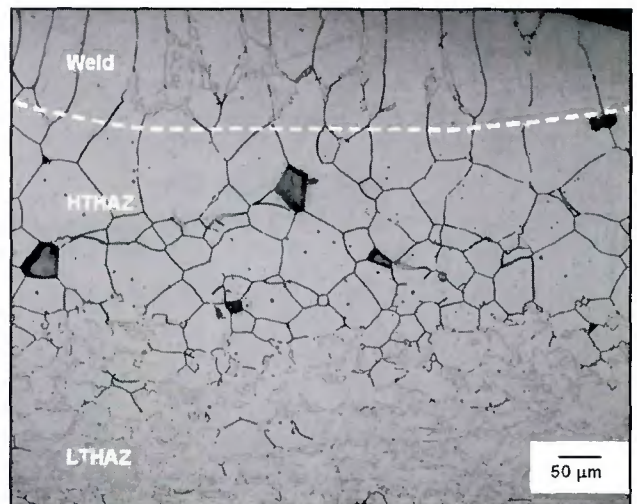


Fig. 6 — Optical photomicrograph of autogenous bead-on-plate weld A2, welded at a heat input of 31.2 J/mm (792 J/in.), and etched electrolytically in 10% oxalic acid. A continuous network of ditched ferrite-ferrite grain boundaries is visible in the high-temperature heat-affected zone.

Table 4 — Summary of the Microstructures Observed in the High-Temperature Heat-Affected Zones of the Experimental Welds after Oxalic Acid Etching

Group	Microstructure	Oxalic acid etch results
1	Predominantly ferritic, with less than half of all grain boundaries containing some martensite	All ferrite-ferrite grain boundaries ditched; ferrite-martensite phase boundaries largely unattacked
2	Predominantly ferritic, with at least half of all grain boundaries containing some martensite	All ferrite-ferrite grain boundaries ditched; ferrite-martensite phase boundaries intermittently attacked
3	Ferritic, with most of the grain boundaries covered in martensite	Localized carbide precipitation on any remaining ferrite-ferrite grain boundaries; ferrite-martensite phase boundaries largely unaffected

for a period of 300 seconds (Ref. 18). At a potential of 0 V_{SCE}, any regions of the microstructure containing more than 10% chromium will be passive, whereas any regions with less than 10% chromium will corrode actively (as shown in Fig. 2). Any chromium-depleted regions will therefore dissolve preferentially. Since it is difficult to accurately measure the area covered by the narrow high-temperature heat-affected zone, a current density value could not be calculated. A microstructural examination of the samples subjected to the test, using optical and scanning electron microscopes, was therefore preferred as a method of evaluation.

In order to determine the influence of welding parameters on the microstructure of the high-temperature heat-affected zone adjacent to the weld interface, point count methods were used to estimate the room-temperature martensite content of each weld. Point counting was performed by randomly moving a grid with four intersecting lines on a series of photomicrographs of the

HTHAZ of each weld, counting all the intersection points located within the martensite phase (counted as one), or on a ferrite-martensite phase boundary (counted as half). A total of eighty counts was performed for each weld. The cooling rate experienced by a point located on the weld interface of each weld as a function of the welding parameters was then calculated using Rosenthal's conduction-driven heat flow model (Ref. 23).

Results and Discussion

Weld Thermal Cycles and HTHAZ Microstructures

Equation 2 can be used to calculate the heat input, *HI*, of each experimental weld from the welding parameters, where *V* is the arc voltage, *I* is the welding current, *v* is the travel speed, and *q* is the weld heat flux. The arc efficiency factor, η , was estimated by comparing the actual *q/v* required to produce a weld with a given weld

pool diameter (measured experimentally), with the heat input calculated from the welding parameters (without considering the arc efficiency factor).

$$HI = \frac{\eta VI}{v} = \frac{q}{v} \quad (2)$$

The average arc efficiency was calculated as 47.76%. This value approaches the upper limit of the range normally quoted for gas tungsten arc welding (between approximately 22 and 48%) (Ref. 24). Electrode negative polarity was used for welding, which focuses the majority of the heat generated by the power source into the workpiece and restricts electrode heating, thereby limiting heat losses through the tungsten electrode and the water-cooled welding torch. The actual heat input during welding, taking into consideration the measured welding parameters and the average arc efficiency factor, was then calculated from equation 2 for each experimental weld. These heat input values are shown in Tables I and II for alloys A and B, respectively.

The martensite content measured in the high-temperature heat-affected zone of each weld is presented graphically in Fig. 3 as a function of the actual heat input during welding. From this figure, it is evident that alloy B formed more martensite than alloy A at corresponding heat input levels. This can be attributed to the higher austenite potential of steel B, denoted by the lower Kaltenhauser ferrite factor listed in Table 2. Figure 3 also shows that the heat-affected zone martensite content of both steels decreases as the heat input during welding is reduced. This reduction in the martensite content of the high-temperature heat-affected zone with de-

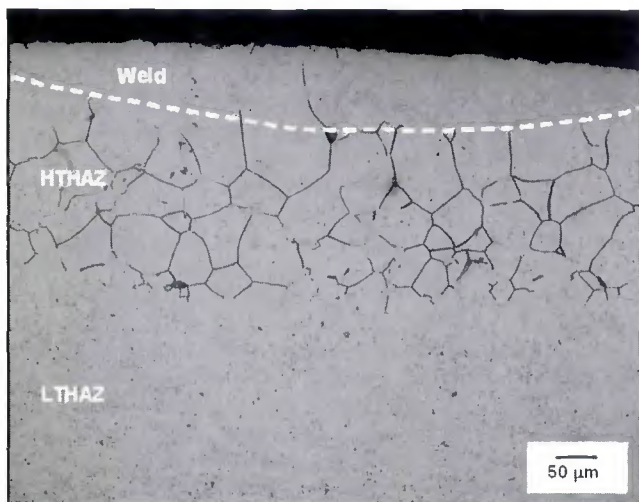


Fig. 7 — Optical photomicrograph of autogenous bead-on-plate weld B2, welded at a heat input of 28.1 J/mm (714 J/in.), and etched electrolytically in 10% oxalic acid. A continuous network of ditched ferrite-ferrite grain boundaries is visible in the high-temperature heat-affected zone.

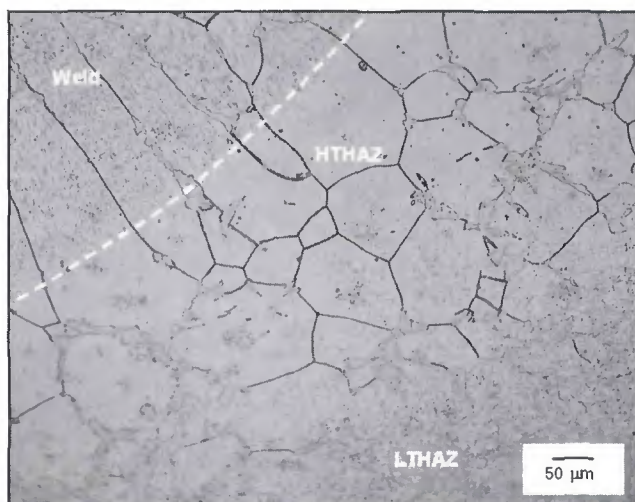


Fig. 8 — Optical photomicrograph of autogenous bead-on-plate weld A13, welded at a heat input of 190.9 J/mm (4849 J/in.), and etched electrolytically in 10% oxalic acid. More grain boundary martensite is present. The ferrite-ferrite grain boundaries are ditched, whereas the ferrite-martensite phase boundaries are largely unattacked.

creasing heat input can be attributed to an increase in the cooling rate after welding.

In order to quantify the influence of the welding parameters, and in particular the heat input, welding speed, and heat flux or power, q , on the cooling rate, Rosenthal's conduction-driven model for heat flow was used to estimate the thermal cycle experienced by a point located on the weld interface during welding. The two-dimensional heat flow model developed by Rosenthal was selected after calculation of the critical thickness for the range of heat inputs used. The weld interface forms between the weld metal and the high-temperature heat-affected zone, and therefore represents the edge of the HTHAZ adjacent to the weld bead. In equation 3, T is the temperature at a radial distance r from the heat source (K), T_0 is the original temperature of the plate prior to welding (K), λ is the thermal conductivity ($\text{Jm}^{-1}\text{s}^{-1}\text{K}^{-1}$), d is the plate thickness (m), a is the thermal diffusivity (m^2s^{-1}), ξ is the distance from the moving point heat source in the direction of travel of the arc ($\xi > 0$ for points in front of the heat source, and $\xi < 0$ for points behind the heat source), and r is the radial distance from the heat source (m). The material constants, λ and a , used in the calculation were supplied by the steel producer and are shown in Table 3.

$$T - T_0 = \frac{q}{2\lambda d \sqrt{\pi r}} \exp\left(-\frac{v(\xi + r)}{2a}\right) \quad (3)$$

The time required for a point located on the weld interface to cool from 1500° to 800°C, Δt_{15-8} , after welding was then estimated from the calculated temperature-

time curves for each experimental weld. The temperature interval from 1500° to 800°C represents the approximate temperature range from the liquidus to a temperature just below the austenite phase field on the phase diagram in Fig. 1, and therefore includes the interval over which the solid-state transformation of ferrite to austenite takes place.

Examples of the calculated temperature-time curves are shown in Fig. 4 for "low," "intermediate," and "high" heat inputs, respectively. These thermal cycles illustrate that an increase in heat input leads to more gradual cooling and a longer cooling time from 1500° to 800°C after welding. Since the solid-state transformation of ferrite to austenite during cooling is nucleation and growth controlled, it is postulated that the faster cooling rates experienced by the high-temperature heat-affected zone during welding at low heat input levels may suppress the transformation to austenite, resulting in lower room-temperature heat-affected zone martensite contents (as illustrated in Fig. 3).

The influence of welding speed, v , and heat flux, q , on the cooling rate experienced by the high-temperature heat-affected zone is presented graphically in Fig. 5, which demonstrates that at comparable values of q , the cooling rate increases with an increase in welding speed.

Sensitization Tests

The Oxalic Acid Electrolytic Etch

The results of the oxalic acid electrolytic etch (Practice W of ASTM 763-93) are summarized in Table 4. In order to

simplify the subsequent discussion of these results, the high-temperature heat-affected zone microstructures revealed by the etch are divided into three groups based on observed similarities in microstructure.

Group 1 refers to as-etched high-temperature heat-affected zone microstructures consisting predominantly of ferrite, with less than half of all grain boundaries containing some martensite. All the ferrite-ferrite grain boundaries are ditched, implying that these boundaries may be in the sensitized condition. The ferrite-martensite phase boundaries are largely unaffected, suggesting that these boundaries are not sensitized. Figures 6 and 7 display optical micrographs of as-etched heat-affected zones with almost no grain boundary martensite. A continuous network of ditched ferrite-ferrite grain boundaries is visible, and etching resulted in isolated incidences of grain dropping. Very little martensite is present in the high-temperature heat-affected zone, and the martensite shows little or no evidence of grain boundary attack during oxalic acid etching.

Group 2 welds contain high-temperature heat-affected zones with at least half of the grain boundaries covered in martensite. In the case of steel A, up to 65%, and in the case of steel B, up to 100% of all the boundaries contain some martensite, as shown in the micrographs in Figs. 8 and 9. The ferrite-ferrite grain boundaries are ditched, but only sporadic attack is visible on the ferrite-martensite phase boundaries. Ditching of the ferrite-ferrite grain boundaries in group 2 indicates that sensitization is possible, but additional tests are required to confirm this. The ferrite-martensite phase boundaries

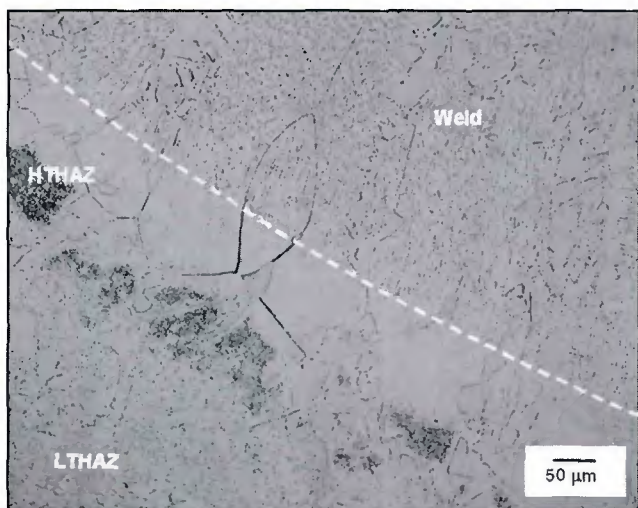


Fig. 9 — Optical photomicrograph of autogenous bead-on-plate weld B13, welded at a heat input of 191.7 J/mm (4869 J/in.), and etched electrolytically in 10% oxalic acid. The majority of the grain boundaries are covered in martensite. Any remaining ferrite-ferrite boundaries are ditched.

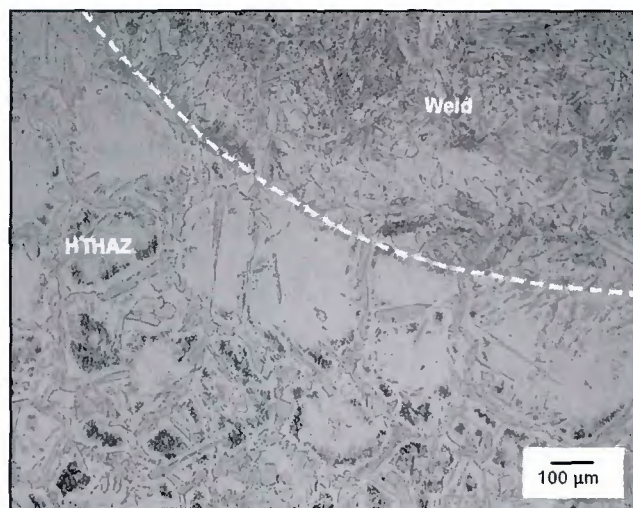


Fig. 10 — Optical photomicrograph of autogenous butt joint weld A25, welded at a heat input of 414.2 J/mm (10521 J/in.), and etched electrolytically in 10% oxalic acid. No ferrite-ferrite grain boundaries are visible.

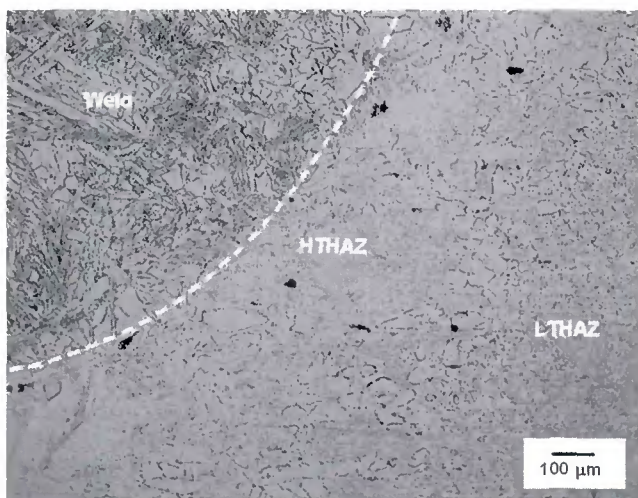


Fig. 11 — Optical photomicrograph of autogenous butt joint weld B25, welded at a heat input of 414.2 J/mm (10521 J/in.), and etched electrolytically in 10% oxalic acid. No ferrite-ferrite grain boundaries are visible.

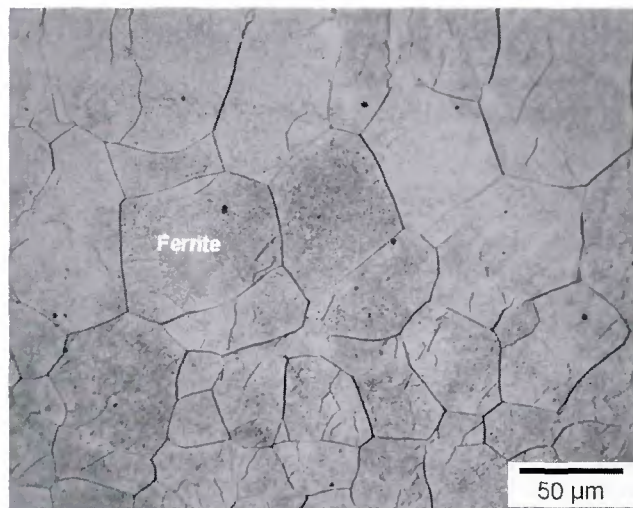


Fig. 12 — Optical photomicrograph of autogenous bead-on-plate weld A2, welded at a heat input of 31.2 J/mm (792 J/in.), after the potentiostatic chromium depletion test. A continuous network of ditched ferrite-ferrite grain boundaries is visible.

are not continuously ditched, and are therefore assumed to be unsensitized.

The high-temperature heat-affected zone grain boundaries of welds in group 3 are not continuously ditched, as illustrated in Figs. 10 and 11. Most of the grain boundaries contain martensite, with martensite covering between 65 and 100% of the total grain boundary area in steel A heat-affected zones, and almost all the grain boundaries in steel B. The absence of continuously ditched grain boundaries indicates that none of these heat-affected zones is sensitized. The potentiostatic chromium depletion test will be used to confirm that the high-temperature heat-affected zone grain boundaries in these

samples are in the unsensitized condition.

Potentiostatic Chromium Depletion Test

The results of the potentiostatic chromium depletion test were found to be in excellent agreement with those of the 10% oxalic acid etch, i.e., the ferrite-ferrite grain boundaries that were ditched during the oxalic acid etch generally also contain continuous chromium-depleted zones. Some of the results are considered below.

At very low heat inputs, where almost no martensite forms in the high-temperature heat-affected zone during cooling, all the ferrite-ferrite grain bound-

aries were etched during the potentiostatic scan. An example of such a high-temperature heat-affected zone is shown in Fig. 12. The presence of etched chromium-depleted zones at the ferrite-ferrite grain boundaries confirms that carbide precipitation during cooling resulted in sensitization of the high-temperature heat-affected zone.

Figure 13 shows the high-temperature heat-affected zone of a weld produced at a slightly higher heat input level, resulting in an increased volume-fraction of grain boundary martensite. The ferrite-ferrite grain boundaries are attacked (and therefore in the sensitized condition), while the phase boundaries between the ferrite and

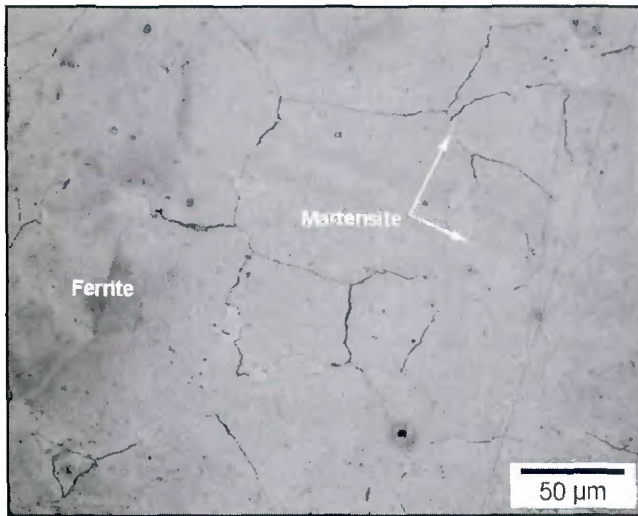


Fig. 13 — Optical photomicrograph of autogenous bead-on-plate weld A11, welded at a heat input of 153.6 J/mm (3901 J/in.), after the potentiostatic chromium depletion test. A discontinuous network of ditched ferrite-ferrite grain boundaries is visible, whereas the ferrite-martensite phase boundaries are largely unattacked.

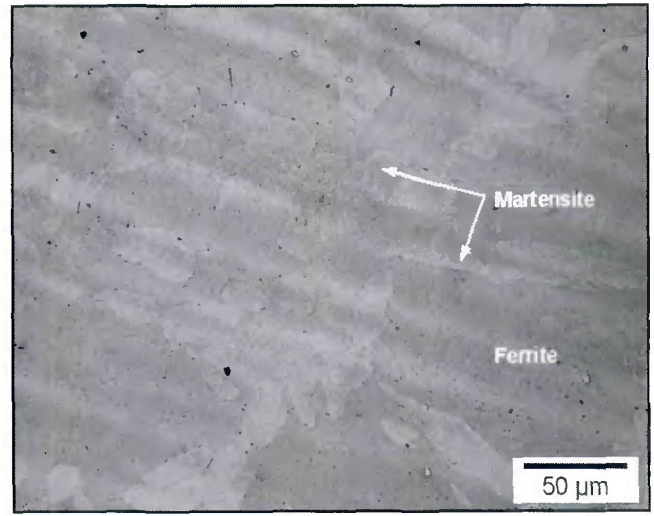


Fig. 14 — Optical photomicrograph of autogenous butt joint weld A18, welded at 262.7 J/mm (6673 J/in.), after the potentiostatic chromium depletion test. No ferrite-ferrite grain boundaries are present.

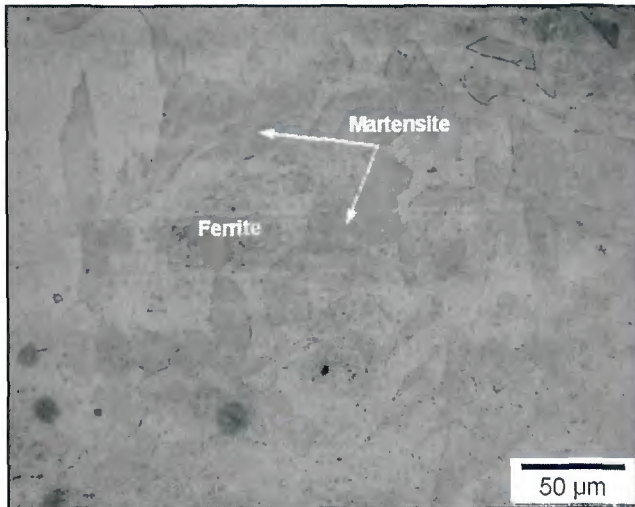


Fig. 15 — Optical photomicrograph of autogenous butt joint weld B15, welded at 250.6 J/mm (6365 J/in.), after the potentiostatic chromium depletion test. No ferrite-ferrite grain boundaries are present.

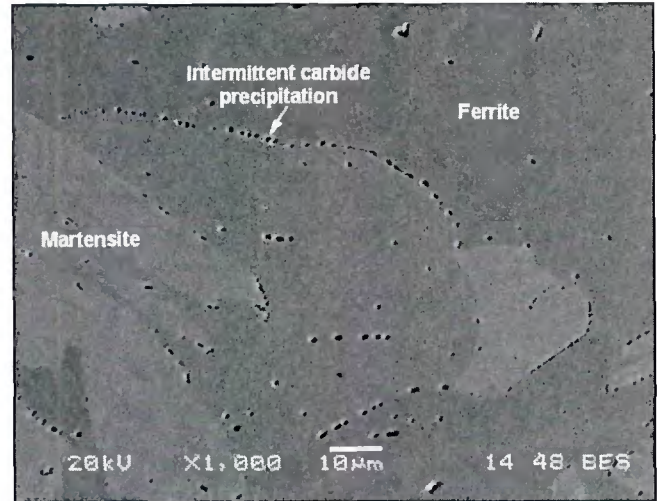


Fig. 16 — SEM photomicrograph of autogenous butt joint weld A18, welded at 262.7 J/mm (6673 J/in.), after the potentiostatic etch. A ferrite-ferrite grain boundary is visible, but it is not continuously ditched.

the lighter martensite phase are largely unattacked, and therefore assumed to be unsensitized.

In welds where the high-temperature heat-affected zone grain boundaries are completely or almost completely covered in martensite, no chromium depletion is evident, as shown in Figs. 14 and 15. This was confirmed by examining these samples using a scanning electron microscope (SEM). The SEM photomicrographs of the heat-affected zones of welds A18 and B13 are shown in Figs. 16 to 19. These welds represent the lowest heat input levels where continuous ferrite-ferrite grain boundaries did not form in the high-temperature heat-affected zones of steels

A and B. Note that in these figures the lighter phase is martensite and the darker phase is ferrite.

Figures 16 and 17 show various regions of weld A18 after the potentiostatic etch. Some evidence of localized chromium depletion is evident in Fig. 16, but attack is not continuous. Most of the grain boundaries in Fig. 17 are covered in martensite and display little evidence of chromium depletion. Two ferrite-ferrite grain boundaries close to the weld interface display evidence of chromium depletion, but it should be noted that a continuous network of ditched ferrite-ferrite grain boundaries is not present in this sample.

Figure 18 shows a large area of weld

B13, including the high-temperature heat-affected zone and part of the low-temperature heat-affected zone. No ferrite-ferrite grain boundaries are visible. Figure 19 displays the high-temperature heat-affected zone at a higher magnification. Only ferrite-martensite phase boundaries are visible, and no chromium depletion is evident in the vicinity of any of these boundaries.

The objective of this investigation was to demonstrate that a single weld can sensitize during continuous cooling after welding. The results described above suggest that this occurs when low heat input welding results in very fast cooling rates. Rapid cooling after welding can suppress

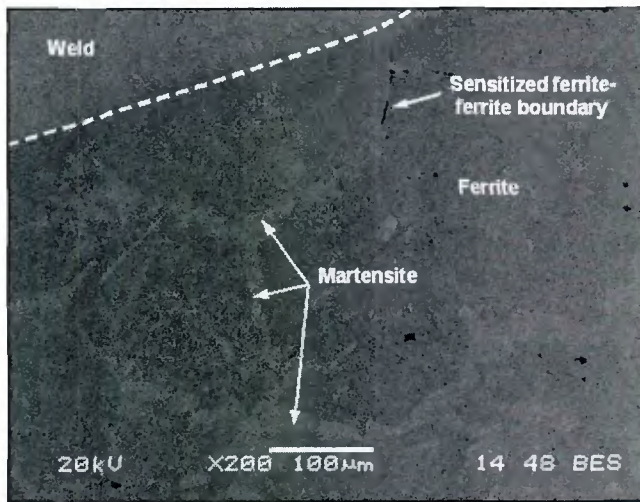


Fig. 17 — SEM photomicrograph of the HTHAZ of autogenous butt joint weld A18, welded at 262.7 J/mm (6673 J/in.), after the potentiostatic etch. Note the isolated ditched ferrite-ferrite grain boundaries close to the weld interface (top, center).

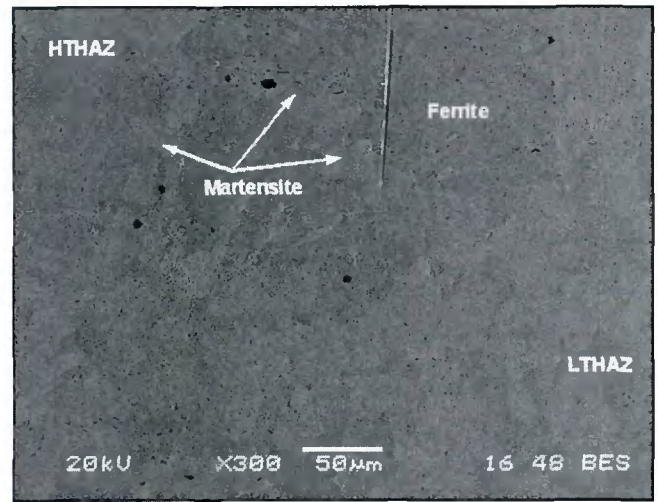


Fig. 18 — SEM photomicrograph of the HTHAZ and the LTHAZ (low-temperature heat-affected zone) of autogenous butt joint weld B13, welded at 191.7 J/mm (4869 J/in.), after the potentiostatic etch. No ferrite-ferrite grain boundaries are present.

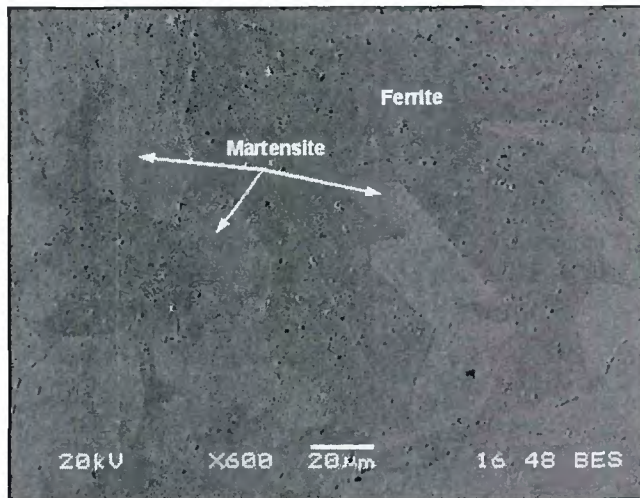


Fig. 19 — SEM photomicrograph of the HTHAZ of autogenous butt joint weld B13, welded at 191.7 J/mm (4869 J/in.), after the potentiostatic etch. No ferrite-ferrite grain boundaries are present.

austenite nucleation as the heat-affected zone cools through the dual-phase (austenite+ferrite) phase field, resulting in almost fully ferritic high-temperature heat-affected zone microstructures. The ferrite phase becomes supersaturated in carbon, and extensive carbide precipitation occurs at the ferrite-ferrite grain boundaries during the cooling. The fast cooling rate also prevents the back-diffusion of chromium to the depleted regions adjacent to the chromium-rich carbides, resulting in a continuous network of sensitized ferrite-ferrite grain boundaries. As the heat input increases, the cooling rate is reduced and more austenite forms in the heat-affected zone. This austenite transforms to martensite at lower temperatures and is retained down to room temperature

as a grain boundary martensite network within the ferritic heat-affected zone. If enough austenite forms on cooling to absorb excess carbon (austenite has a higher carbon solubility than ferrite), a continuous network of chromium-depleted zones does not form and sensitization is prevented. Slower cooling after welding at higher heat input levels also allows the ferrite phase to desensitize through diffusion of chromium from the grain interiors into any chromium-depleted zones.

Due to its higher austenite potential, steel B formed more martensite in the high-temperature heat-affected zone than steel A after welding at comparable heat input levels. In steel B almost continuous networks of martensite were observed on the high-temperature heat-affected zone grain boundaries of all welds produced at heat inputs of 192 J/mm (4877 J/in.) or higher, corresponding to cooling rates of 293°C/s or less. In steel A, continuous ferrite-ferrite grain boundaries were only eliminated at heat inputs of 263 J/mm (6680 J/in.) (corresponding to a cooling rate of 85°C/s) or higher. In welds produced at higher heat input levels, continuous ferrite-ferrite grain boundaries were virtually eliminated, and the heat-affected zones were shown to be unsensitized.

Conclusions

This investigation studied the sensitization of two type EN 1.4003 ferritic stainless steels during continuous cooling after welding. Based on the results obtained, the following conclusions can be drawn:

- Sensitization of type EN 1.4003 ferritic stainless steels during continuous cooling after welding is possible if low heat input levels are used.
- Welding at low heat inputs can suppress the transformation of ferrite to austenite as the heat-affected zone cools through the (austenite+ferrite) dual-phase region during welding. This results in largely ferritic high-temperature heat-affected zones.
- Carbon supersaturation of the ferrite phase occurs in the absence of sufficient austenite during cooling, resulting in extensive carbide precipitation on the ferrite-ferrite grain boundaries. Chromium back-diffusion is prevented by rapid cooling, and the ferrite-ferrite grain boundaries are sensitized to intergranular corrosion.
- With an increase in heat input, the cooling rate after welding is reduced, and more austenite forms in the high-temperature heat-affected zone. Sensitization is prevented by the presence of enough austenite to eliminate continuous ferrite-ferrite grain boundaries.
- Due to its higher austenite potential, steel B contained more martensite than steel A in the high-temperature heat-affected zone after welding at comparable heat input levels. A sufficiently high austenite potential should be maintained in these steels to promote austenite formation during cooling. In this respect, a reduction in carbon content or an increase

in the amount of ferrite-forming elements in type EN 1.4003 steels needs to be balanced by the addition of austenite-forming elements such as nickel.

- Excessive welding speeds appear to exacerbate sensitization during low heat input welding.

In addition to specifying a maximum heat input for welding the EN 1.4003 steels (to limit heat-affected zone grain growth), guidelines supplied to fabricators should include a minimum recommended heat input level. This minimum heat input will be a function of the plate thickness and chemistry, but 300 J/mm appears to be an appropriate limit for 3-mm plate. Heat flow modeling can be used for different chemistries to calculate appropriate minimum heat input levels for various plate thicknesses. A maximum weld interface cooling rate of 80°C/s ($\Delta t_{15-8} = 8.75$ s) can be used as a preliminary guideline to distinguish between heat inputs likely to cause sensitization, and those where cooling after welding is slow enough to prevent the formation of continuous chromium-depleted zones. Guidelines should also emphasize the harmful effect of fillet weld overlap (most welding standards limit the amount of allowable overlap) and excessive welding speeds.

Acknowledgments

The authors would like to thank Columbus Stainless and THRIP for sponsoring the project and the University of Pretoria for providing laboratory facilities. The assistance of Prof. P. C. Pistorius and Prof. G. T. van Rooyen is also gratefully acknowledged.

References

1. *3CR12 - The Utility Stainless Steel*. 1997. Technical manual published by Columbus Stainless.
2. *3CR12 - Technical Data*. 2004. Technical manual published by Columbus Stainless.
3. Maxwell, D. K., Warrington, J., and Dewar, K. 1993. From niche to commodity, 3CR12 - a ten-year scenario. *Corrosion Reviews* 11(3-4): pp. 17-32.
4. Grobler, C. 1987. Weldability studies on 12% and 14% chromium steels. PhD dissertation, University of Pretoria, South Africa.
5. Meyer, A. M. 2000. Interstitial diffusion from the weld metal into the high temperature heat affected zone in 11 - 12 percent chromium steel welded joints. MEng thesis, University of Pretoria, South Africa.
6. Folkhard, E. 1988. *Welding Metallurgy of Stainless Steels*. Springer-Verlag, Vienna: p. 11.
7. Matthews, L. M., Griesel, B., Longman, P. T., Van Rooyen, G. T., and Prozzi, J. M. 1999. Sensitisation in low-carbon 12% chromium containing stainless steels. *Proceedings of the 14th International Corrosion Congress*. Cape Town, South Africa: p. 332.
8. Bavarian, B., Szklarska-Smialowska, Z.,

and MacDonald, D. D. 1982. Effect of temperature on the stress corrosion cracking of tempered type 403 martensitic stainless steel in sodium sulfate solution. *Corrosion* 38(12): pp. 604-608.

9. Nishimura, R. 1992. Stress corrosion cracking of type 430 ferritic stainless steel in chloride and sulfate solutions. *Corrosion* 48(11): pp. 882-890.

10. Frangini, S. 1994. Sensitivity to stress corrosion cracking of type 405 stainless steel in high-temperature aqueous environments. *Corrosion* 50(6): pp. 447-456.

11. Cihal, V. 1984. Intergranular Corrosion of Steels and Alloys. *Material Science Monographs*, 18. Elsevier: pp. 79-83.

12. Solomon, H. D., and Devine, T. M. 1984. Duplex stainless steels - A tale of two phases. *Proceedings of Duplex Stainless Steels*. St. Louis, Mo.: pp. 693-756.

13. Tuling, A. 2001. EELS study of sensitisation in 12% chromium steel. *Proceedings of the Microscopy Society of Southern Africa* 31: p. 26.

14. Tomari, H., Fujiwara, K., Shimogori, K., Fukuzuka, T., and Kanda, M. 1982. Intergranular stress corrosion cracking of 13% Cr and 18% Cr ferritic steels in high temperature high purity water. *Corrosion* 38(5): pp. 283-294.

15. Frangini, S., and Mignone, A. 1992. Modified electrochemical potentiokinetic reactivation method for detecting sensitisation in 12 wt-% chromium ferritic stainless steels. *Corrosion* 48(9): pp. 715-726.

16. Kaltenhauser, R. H. 1982. *Source Book on the Ferritic Stainless Steel*. ASM Engineering Bookshelf: pp. 212-218.

17. ASTM A763-93 (2004). *Standard Practices for Detecting Susceptibility to Intergranular Attack in Ferritic Stainless Steels*. ASTM International.

18. Pistorius, P. C., and Coetzee, M. 1996. Sensitization of 430 ferritic stainless steel during continuous annealing. *Journal of the South African Institute of Mining and Metallurgy* 96(3): pp. 119-125.

19. Rocha, H. J., and Lennartz, G. 1955. The activation potential of iron-chromium alloys and its relationship to the sulfur content of these alloys. *Archives of Eisenhüttenwese* (26): pp. 117-123.

20. King, P. F., and Uhlig, H. H. 1959. Passivity in the iron-chromium binary alloys. *Journal of Physical Chemistry* 63: pp. 2026-2032.

21. Frankenthal, R. P., and Pickering, H. W. 1973. Intergranular corrosion of a ferritic stainless steel. *Journal of the Electrochemical Society* 120: pp. 23-26.

22. Kirchheim, R., Heine, B., Fischmeister, H., Hofmann, S., Knotz, H., and Stolz, U. 1989. The passivity of iron-chromium alloys. *Corrosion Science* 29: pp. 889-917.

23. Rosenthal, D. 1946. The theory of moving sources of heat and its application to metal treatments. *Transactions of the AIME* 68: pp. 849-866.

24. Easterling, K. 1992. *Introduction to the Physical Metallurgy of Welding*, 2nd Edition, Butterworth-Heinemann: p. 19.

Appendix

Table I — Welding Parameters Measured for Steel A during Autogenous Gas Tungsten Arc Welding

Weld number	Welding current A	Arc voltage V	Welding speed mm/s	Heat input J/mm
A1	168	14	33.3	33.7
A2	109	10	16.7	31.2
A3	38	10	4.94	36.7
A4	222	14	33.3	44.6
A5	130	10	16.7	37.2
A6	50	9	4.94	43.5
A7	352	19	33.3	96.7
A8	223	15	16.7	95.7
A9	91	10	4.94	88.0
A10	301	16	16.7	137.7
A11	189	14	8.23	153.6
A12	125	10	4.94	120.9
A13	272	17	11.57	190.9
A14	210	16	8.23	195.0
A15	144	13	4.94	181.0
A16	252	17	8.23	248.6
A17	168	13	4.94	211.1
A18	118	11	2.36	262.7
A19	199	15	4.94	288.6
A20	127	12	2.36	308.4
A21	219	16	4.94	338.8
A22	135.5	12	2.36	329.1
A23	236	16	4.94	365.1
A24	146	13	2.36	384.1
A25	252	17	4.94	414.2
A26	164	13	2.36	431.5

Table II — Welding Parameters Measured for Steel B during Autogenous Gas Tungsten Arc Welding

Weld number	Welding current A	Arc voltage V	Welding speed mm/s	Heat input J/mm
B1	168	13	33.3	31.3
B2	109	9	16.7	28.1
B3	38	9.5	4.94	34.9
B4	222	16	33.3	50.9
B5	130	10	16.7	37.2
B6	50	9	4.94	43.5
B7	352	20	33.3	101.0
B8	223	15	16.7	95.7
B9	91	10	4.94	88.0
B10	301	16	16.7	137.7
B11	190	15	8.23	165.4
B12	125	10	4.94	120.9
B13	273	17	11.56	191.7
B14	210	16	8.23	195.0
B15	144	18	4.94	250.6
B16	252	17	8.23	248.6
B17	168	14	4.94	227.4
B18	118	10	2.36	238.8
B19	199	15	4.94	288.6
B20	127	12	2.36	308.4
B21	219	16	4.94	338.8
B22	135.5	12.5	2.36	342.8
B23	236	16	4.94	365.1
B24	146	13	2.36	647.2
B25	252	17	4.94	414.2
B26	165	13	2.36	434.1